

Interpretable Neural Networks for Predicting Mortality Risk using Multi-modal Electronic Health Records

Alvaro E. Ulloa Cerna^{*†}, Marios Pattichis[†], *Senior Member, IEEE*, David P. vanMaanen^{*}, Linyuan Jing^{*}, Aalpen A. Patel^{*‡}, Joshua V. Stough^{**}, Christopher M. Haggerty^{*¶}, and Brandon K. Fornwalt^{*‡¶}

^{*}Department of Imaging Science and Innovation, Geisinger, PA 17822 USA

[†]Department of Electrical and Computer Engineering, University of New Mexico, NM 87106, USA

[‡]Department of Radiology, Geisinger, PA 17822, USA [¶]The Heart Institute, Geisinger, PA 17822, USA

Abstract—We present an interpretable neural network for predicting an important clinical outcome (1-year mortality) from multi-modal Electronic Health Record (EHR) data. Our approach builds on prior multi-modal machine learning models by now enabling visualization of how individual factors contribute to the overall outcome risk, assuming other factors remain constant, which was previously impossible.

We demonstrate the value of this approach using a large multi-modal clinical dataset including both EHR data and 31,278 echocardiographic videos of the heart from 26,793 patients. We generated separate models for (i) clinical data only (CD) (e.g. age, sex, diagnoses and laboratory values), (ii) numeric variables derived from the videos, which we call echocardiography-derived measures (EDM), and (iii) CD+EDM+raw videos (pixel data). The interpretable multi-modal model maintained performance compared to non-interpretable models (Random Forest, XG-Boost), and also performed significantly better than a model using a single modality (average AUC=0.82). Clinically relevant insights and multi-modal variable importance rankings were also facilitated by the new model, which have previously been impossible.

I. INTRODUCTION

The adoption of Electronic Health Records (EHR) in medicine has facilitated the collection of massive amounts of clinical data which can be used to develop highly accurate risk models that physicians can use to guide medical decision making. To take full advantage of the available EHR data, these models, similar to a physician, need to be able to handle multiple modalities as inputs. For example, both tabular data such as laboratory measurements and pixel data from clinical images should be readily incorporated. This basic framework is shown in Fig. 1.

As documented in [1], [2], [3], [4], precision medicine can benefit greatly from development of these risk models. The proliferation of these models has prompted scrutiny from the medical community, which demands clinical validity and interpretability to improve usefulness [5] and inclusion of all relevant predictors (or, conversely, explanation when a relevant data input is excluded) [6]. Moreover, the recent European General Data Protection Regulation (<https://eugdpr.org/>) states that individuals who have decisions made about them by algorithms have a right to know the basis of the decision and

the factors that influenced this decision. Thus, any medical risk model should be interpretable and facilitate understanding of the various contributions of different inputs towards the overall risk assessment.

When only using tabular EHR data, clinical interpretability is well supported by linear models. To see this, note that the coefficients of the different predictors can be used to assess feature importance based on the magnitude of each coefficient, and effect directionality based on the sign. Unfortunately, the performance of linear models can be limited. As described in [1], for predicting mortality risk using EHR data, non-linear models such as random forests outperform linear models. While not as direct as for linear models, there are also approaches to support clinical interpretability for non-linear methods. As an example, for ensemble methods based on decision trees (e.g., Random Forests), we can rank the input features based on the proportion of samples that appear at each decision node where each feature is used. Unfortunately, there is no direct explanation for the input effect. Currently, methods to support clinical interpretability include building a single tree with multivariate decision nodes [7], extracting an optimal tree with a minimum performance cost [8], and an indirect method that offers recommendations for transforming true negative instances into positively predicted ones [9]. However, the ability to expand such interpretable models to more robust, multi-modal frameworks—capable of ingesting all the diverse and heterogeneous elements of EHR data, such as digital images and videos—has been challenging. To date, no such model has been developed.

A major challenge in developing interpretable multi-modal models for clinical use is that non-interpretable deep learning methods dominate research on data such as medical images [10] and tabular EHR data [11]. To particularly highlight the capabilities of deep learning in medical imaging analysis, such methods have been used in ultrasound video analysis for frame labeling tasks such as segmentation of certain chambers of the heart (the left ventricle) [12], [13], fetal standard image plane / orientation detection [14], [15], and echocardiographic video classification tasks [16]. Given this success, there is clear need to explore/develop interpretable frameworks that are compatible with deep learning models.

Interpreting deep learning models remains complicated.

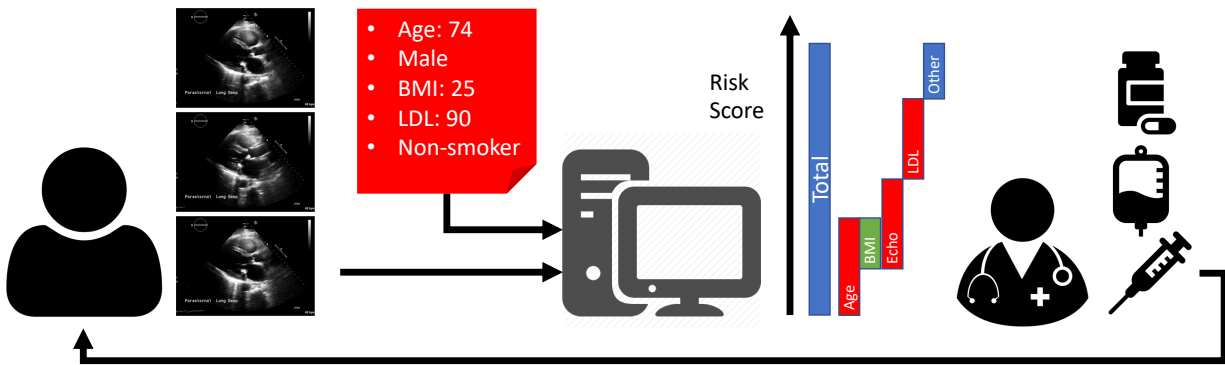


Fig. 1: General framework for multimodal risk assessment. EHR data and cardiac ultrasound videos are input to the risk assessment system. We emphasize the use of separable non-linear models where we look at contributions from each modality and each feature separately and also within the joint multimodal framework. The mortality risk assessment is used to inform treatment.

Nevertheless, significant progress has been made as documented in section VI of [11]. There, the authors list well accepted methods such as maximum activation, imposing constraints, qualitative clustering, and a mimic learning method that approaches deep learning performance using a gradient boosting tree. Unfortunately, maximum activation is impractical for global interpretations since there is a very large number of internal neurons that can be maximized. Imposing constraints can limit the search space and help interpretability. As we shall see, we will also impose non-negativity constraints to resolve ambiguities. For image analysis applications, two additional approaches to support interpretability have been introduced. First, for convolutional neural network (CNN) based methods, we can look at the output images from each pool layer to understand how the CNN performs feature extraction at different levels. Second, more recently, there is an effort to support interpretability by using CNNs to perform semantic segmentation. The basic approach described in Fully Convolutional Networks (FCN) [17], SegNet [18], and U-net [19], is to use an auto-encoding structure that predicts class labels of each pixel by using a transposed version of a traditional CNN architecture. Yet, large scale semantic labeling of big datasets, such as those available in the EHR, is intractable.

Clinical interpretation of the importance of deep learning features is considerably more challenging. Early efforts to provide feature importance have been reported by Gevrey et. al in [20]. In classical stepwise selection, feature importance is assessed based on performance changes. More directly, we can use the partial derivative of the output with respect to a specific input feature to assess their linear dependency. In this case, a positive partial derivative implies that an increase in the input feature value will also result in an increase in the output. On the other hand, a negative partial derivative indicates that an increase in the feature will result in a reduction of the output. More recently, Ribiero et al. [21] proposed feature ranking by learning a Local Interpretable Model (LIME) that is agnostic to the classifier. Depending on the underlying classifier, examples of a local interpretable model include a linear model or a single decision tree that capture the behavior of the classifier

for small variations of the input.

Both the partial derivative and the LIME approaches cannot provide global descriptions of the input effects. To understand this problem, we note that local linear models can vary significantly from sample to sample. Hence, when using LIME or partial derivatives, there is a need to specify all of the inputs and then fit the local linear model to the specific patient. Estimating global trends is therefore impossible. As a result, it is not clear how to model the effects of what happens when there are dramatic changes due to effective treatment or substantial changes in lifestyle.

To support the development of clinically interpretable models, we propose a deep learning architecture comprising separable models. Our basic approach is to consider polynomial transformations of each scalar input factor separately and then use a simple weighted sum to combine their contributions—along with other inputs, including video, binary, or continuous variables—for predicting mortality risk. This approach has several advantages. First, we can use the weights to assess the importance of each scalar factor. Second, we can provide a global assessment of the contribution of each scalar factor by simply zeroing out the weights of the remaining factors. In other words, by using separable models, global effects can be modeled for each scalar factor independently.

Here, we demonstrate the value of this approach by applying it to several different types of multi-modal input datasets with the goal of predicting the risk of 1-year mortality after echocardiography. We utilize three different sets of input variables: (i) clinical data (CD) only (e.g. age, sex, diagnoses and laboratory values) (ii) numeric variables derived from echocardiography videos, which we call echocardiography-derived measures (EDM), and (iii) CD+EDM+raw videos (pixel data from the parasternal long axis view), as described in [16]. By considering models that utilize different variable inputs, we can investigate the contributions of each modality separately. For example, by comparing predictions derived using EDM only against the results from video analysis, we establish that EDM are just as effective for risk assessment (we note that this utilized only a single video out of more than 30 that are typically acquired during an echocardiogram

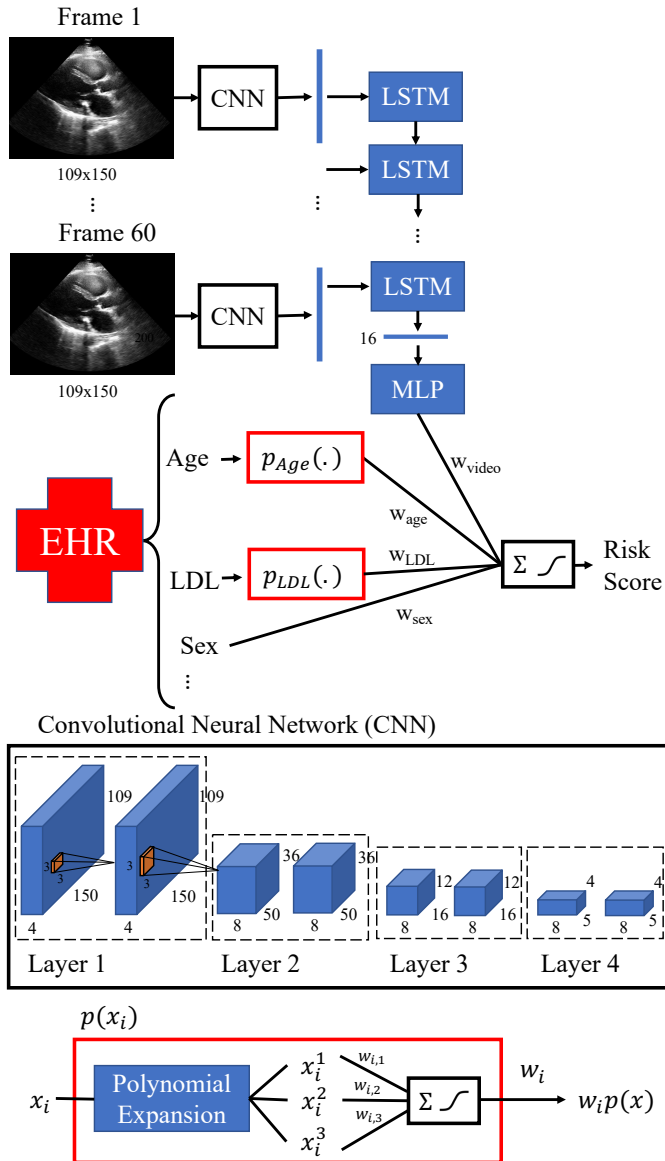


Fig. 2: Architecture of the proposed multi-modal system. The top portion shows the video analysis system and how it produces a scalar output that is input to the sigmoid activation function. The bottom part shows the nonlinear, separable model where the EHR factors are transformed by polynomials and input to the same sigmoid.

and used to derive the “EDM” inputs). On the other hand, we also establish that risk assessment based on multiple modalities significantly outperforms predictions based on any single modality. Furthermore, multimodality feature ranking provides a quantitative assessment of how features from each modality contribute to optimal risk assessment.

The remainder of the paper is organized into four additional sections. In section II, we describe the proposed methodology while in section III we describe the dataset. We then provide results and discussion in section IV and concluding remarks in section V.

II. METHODS

We present the overall architecture in Fig. 2. The multi-modal data are broken into the Echocardiography videos from the parasternal long axis view; 100 scalar clinical variables including 90 cardiovascular-relevant ICD-10 codes, age, sex, height, weight, heart rate, blood pressures, LDL, HDL, and smoking status; and 49 echocardiography derived measurements (EDM), which are numbers measured from the image data by clinicians or technologists. We refer to the supplemental material of [1] for a detailed description of the input variables. We process the data to produce a risk score that represents the likelihood of mortality within a year of the echocardiogram.

The Echocardiography video is separated into individual 2D image frames where each frame is input to a CNN with their outputs input to LSTM cells to capture temporal dependencies across the frames. To support consistency in the learned parameters, the video represents approximately two cycles (exactly 2 seconds) of the heart beat acquired at the parasternal long axis view, sampled at 30 frames per second at a resolution of 109×150 pixels, and starting at the peak of the R-wave of the electrocardiographic QRS complex. The parasternal view contains elements of the left ventricle, left atrium, right ventricle, aortic and mitral valves within a single view. This view also potentially includes pericardial or left pleural effusion, and is thus a highly informative video that is typically the first acquired during a clinical echocardiogram. We provide a detailed description of the video analysis system in section II-A.

At the top level, we combine the results from the different subsystems to produce a single score. For the EHR variables, we use separable, polynomial transformations to transform each continuous or categorical variable independently. We provide a detailed description of the transformations and the different models in section II-B.

In subsection II-C, we interpret the proposed methodology for ranking feature by risk association. We carefully describe how we train, test, and validate the models in II-D. We will later demonstrate our recommendations for interpreting the variables in section IV.

A. Video risk model

We describe the proposed architecture in Table I and Fig. 2. Alternative designs were also considered as described in the ArXiv document given in [16]. The chosen architecture gave optimal results when tested for four different image resolutions, the addition of optical flow feature maps, and for alternative echocardiographic image planes/views other than the parasternal long axis view [16].

The input consists of a video with 60 image frames with 109×150 pixels per image. Each video frame was processed through the CNN architecture shown in the middle of Fig. 2. The CNN consists of four ConvNet layers (L1 to L4). Within each ConvNet, we have two convolution sub-layers with rectified linear unit (ReLU) activations. Thus, Conv1 takes a single frame as an input and produces four feature maps. Then, each Conv1 feature map is further processed by

TABLE I: CNN architecture with 4,237 trainable and 56 non-trainable parameters. Refer to Fig. 2 for the dimensions of the convolution layers. L1, L2, L3, and L4 refer to the four convolution layers shown in the middle diagram of Fig. 2. Each CNN has a single image frame of 109×150 pixels as input. All convolution layers use 3×3 kernels. We use the term “group of feature maps” to refer to the collections of feature maps shown in Fig. 2.

Layer	# Parameters	Description
Input	-	60x109x150 gray scale video
L1: Conv1+ReLU	40	4 2D feature maps
L1: Conv2+ReLU	148	4 groups of feature maps
L1: Batch norm.	16	Normalize feature map groups
L1: Max Pool	-	3x3 max-pooling
L2: Conv3+ReLU	296	8 groups of feature maps
L2: Conv4+ReLU	584	8 groups of feature maps
L2: Batch norm.	32	
L2: Max Pool	-	3x3 max-pooling
L3: Conv5+ReLU	584	8 groups of feature maps
L3: Conv6+ReLU	584	8 groups of feature maps
L3: Batch norm.	32	
L3: Max Pool	-	3x3 max-pooling
L4: Conv7+ReLU	584	8 groups of feature maps
L4: Conv8+ReLU	584	8 groups of feature maps
L4: Batch norm.	32	
L4: Max Pool	-	3x3 max-pooling
LSTM	544	8 hidden units
LSTM	208	4 hidden units
Dense+ReLU	20	4 hidden units
Output+Sigmoid	5	1 output unit

four Conv2 filters to produce a $4 \times 109 \times 150$ feature map (see Fig. 2). We normalize each feature map group with a batch normalization layer. For batch normalization, we have two learnable parameters (β, γ), and two non-learnable parameters (μ, σ) that are computed during runtime as given in [22]. Thus, we have $4 \times 4 = 16$ parameters for Batch normalization for L1. The feature maps are then passed through a Max pool layer applied to each image to reduce the resolution of each by a factor of 3. Similar connections apply for L2, L3, and L4 as shown in Fig. 2 and Table I. The CNN output for each frame is 8 feature maps.

We use two LSTM layers to process the CNN outputs. The CNN outputs from each frame form a time-sequence input to an LSTM layer with 8 hidden units. Then the output of this LSTM layer is input to another LSTM layer with 4 hidden units. The final output is a 4-dimensional vector that is processed through a fully connected layer to a single sigmoid activation (see Table I).

B. Multi-modal Models for Mortality Risk Prediction

In order to integrate clinical features from multiple modalities, we differentiate between categorical factors (e.g., sex), continuous clinical factors (e.g., age), and a video risk factor. Here, we emphasize the special importance of clinical factors that have played a traditional role in diagnosis as opposed to a video risk factor that does not have a clear and well understood clinical interpretation within the context of a risk model. Furthermore, to assess the effects of the different modalities, we construct models based on three different sets of variables. First, we consider single modality models based on: (i) CD

only (ii) EDM only, and (iii) an echocardiography video from parasternal long axis view, which does not include any other measurements. Second, we consider a hierarchy of multimodal models starting from CD data without EDM, adding EDM, and then adding the results from video analysis as well.

We begin by defining all of the variables. Let the list of r scalar clinical factors that exclude EDM be given by $X_s = [x_1, x_2, \dots, x_r]^T$ and let $m_s(X_s)$ denote the single modality model based on them. Similarly, let the EDM variables be given by: $X_v = [x_{r+1}, x_{r+2}, \dots, x_{r+v}]$ with $m_v(X_v)$ as the corresponding model. For the video analysis system, let V denote the input video and let $m_V(V)$ denote the video analysis system described in section II-A.

We consider polynomial transformations applied to each scalar factor separately as given by: $P(X_s) = [p_1(x_1), p_2(x_2), \dots, p_r(x_r)]^T$ and similarly for $P(X_v)$. We use a weighted sum of the contributions from each polynomial based on:

$$W_s^T P(X_s) = w_1 p_1(x_1) + w_2 p_2(x_2) + \dots + w_r p_r(x_r) \quad (1)$$

that satisfy

$$W_s = [w_1, w_2, \dots, w_r], \forall w_i \geq 0, \quad (2)$$

and similarly for $W_v^T X_v$. Here, we require positive weights to eliminate any model ambiguities since $w_i p_i(x_i)$ and $-w_i(-p_i(x_i))$ represent the same term. For binary variables, we simplify $W_b^T P_b(X_b) = W_b^T X_b$ and remove the non-negative constraint for W_b .

For each modality, we consider a sigmoid for modeling the risk likelihood. We thus have that the CD scalar and EDM models are given by:

$$m_s(X_s) = \sigma(W_s^T P(X_s) + b_s) \quad (3)$$

$$m_v(X_v) = \sigma(W_v^T P(X_v) + b_v) \quad (4)$$

where b_s, b_v represent bias terms, and $\sigma(\cdot)$ represents the sigmoid function. We use a binary cross-entropy cost function to train the different models and learn the polynomial weights, coefficient weights, and bias terms.

For the hierarchical, multi-modality models, we consider the original scalar model ($m_s(X_s)$), a second model that also considers EDM: $m_{sv}(\cdot)$, and the full multi-modality model: $m_{svV}(\cdot)$. To simplify the notation, we use the same weight variables to define $m_{sv}(\cdot)$ and $m_{svV}(\cdot)$ as given by:

$$m_{sv}(X_s, X_v) = \sigma(W_s^T P(X_s) + W_v^T P(X_v) + b_{sv}) \quad (5)$$

$$m_{svV}(X_s, X_v, V) = \sigma(W_s^T P(X_s) + W_v^T P(X_v) + w_V^T V + b_{svV}) \quad (6)$$

where b_{sv}, b_{svV} represent bias terms, and the weights W_s, W_v, w_V will need to be learned for the new models.

C. Interpretable Models

We provide interpretation of the proposed methodology based on separability that allows comparisons among the multi-modal input features, whether scalar, binary or video. We begin with interpreting the contributions of scalar features. We then proceed with looking at the relative importance of the different features within the different models.

Each scalar feature contributes to the overall mortality risk through its corresponding coefficient weight that is then input to a logistic regression layer,

$$m_s(X_s) = \frac{1}{1 + \exp(-W_s^T(P(X_s) + b_s))} \quad (7)$$

that gives a risk score. Since we are using the logistic regression $\sigma(\cdot)$, from $\sigma(\text{logit}(p_{\text{mort}})) = p_{\text{mort}}$, where p_{mort} represents the event probability, we have:

$$\begin{aligned} W_s^T P(X_s) + b_s &= \text{logit}(p_{\text{mort}}) \\ &= \log\left(\frac{p_{\text{mort}}}{1 - p_{\text{mort}}}\right) \end{aligned} \quad (8)$$

where $p_{\text{mort}}/(1 - p_{\text{mort}})$ represents the odds ratio for the event. We say that the product $W_s^T P(X_s) + b_s$ represents the log-odds of a mortality event [23]. To understand the risk contribution for the i -th feature, we exponentiate both sides of eq. (8) to eventually derive:

$$\text{Odds-ratio} = C \cdot \exp(w_i p_i(x_i)) \quad (9)$$

where C represents contributions from the rest of the features. From eq. (9), we can see how the weight magnitude can be used to quantify specific feature contributions to the odds ratio. We will refer to eq. (9) in the results.

We rank the importance of each feature by simply ranking the corresponding weights: $w_{(1)} \geq w_{(2)} \geq \dots \geq 0$. Here, it is important to note that eq. (9) describes the contribution of each factor over the entire range of possible values. In other words, it is not a local model that is specific to small changes of a given patient. Instead, large-scale changes can be described by looking at the change from $\exp(w_i p_i(x_i))$ to $\exp(w_i p_i(x_i + \Delta x_i))$ where Δx_i is used to describe a large change in x_i .

To understand the contributions from the video measurements, we rely on the joint interpretation of our hierarchical models: $m_s(\cdot), m_{sv}(\cdot), m_{sv}(\cdot)$. As long as the different models contribute information associated with the label, we expect the performance to follow the hierarchy with $m_{sv}(\cdot)$ giving the best results, followed by $m_{sv}(\cdot)$, and then either of $m_s(\cdot), m_v(\cdot)$, or $m_v(\cdot)$. The relative improvement in performance can be attributed to the added information in each model. Thus, the performance improvement of $m_{sv}(\cdot)$ over $m_s(\cdot)$ is directly attributed to the inclusion of EDM. Similarly, a performance improvement of $m_{sv}(\cdot)$ over $m_{sv}(\cdot)$ implies that the video analysis system is extracting important features that are currently not fully described by the EDM included in $m_{sv}(\cdot)$. Here, we note that a substantial improvement of $m_{sv}(\cdot)$ over $m_{sv}(\cdot)$ may imply that the current clinical EDM are incomplete. On the other hand, the lack of a substantial improvement may be due to the fact that the video processing system was unable to provide new information that could surpass the standard EDM that we are already making, on the context of one-year mortality prediction. Moreover, potential lack of improvement in this scenario could also be due to the fact that we are only including one video out of an average of 20-40 videos acquired per clinical echocardiogram due to computational limitations.

Beyond performance improvements, we look at changes in weights and weight rankings to assess the importance of each feature from each modality. Performance changes reflect

contributions from each modality as a whole, while weight rankings reflect the relative importance of each feature against all others. The presence of high-ranking features from all modalities implies that each modality is making a significant contribution. Further, the relative rankings also matter. For example, the presence of video that ranks higher than echocardiography measurements implies that the video score contains information already given by EDM but within a simpler, single number. Similarly, weight rank changes between models can offer strong clues about the inter-relationships between clinical factors and different modalities.

We also compare our separable non-linear models against generalized linear models (logistic regression models) and non-separable non-linear models such as Random Forest [24] and its extension in XGBoost [25]. Clearly, to justify the use of non-linear models, we expect our models to perform better than the generalized linear model. Then, we expect to be able to provide clinical interpretability without a significant sacrifice in performance. We refer to section IV to see that this is indeed what we found.

D. Training, Validation, and Testing

To estimate the performance of the different models, we performed 5 independent runs. For each run, the dataset was broken into a training set, a validation set, and the test set. We train over the training and validation sets. We report the results over the 5 test sets.

For each run, we used 80% of the dataset for training and validation and the remaining 20% for testing. Within the 80% reserved for training and validation, we used 10% (8% of the original dataset) for validation and the rest for fitting. The training and test sets had the same prevalence of dead vs alive (see Table II of section III). For the validation set, we used a balanced proportion of 50% for each class of Table II.

We normalize each feature by mapping its minimum value to -1 and the maximum value to +1 on the training set using:

$$x_{i,\text{nor}} = 2 \cdot \frac{(x_i - \min(x_i))}{(\max(x_i) - \min(x_i))} - 1 \quad (10)$$

Then, we apply eq. (10) to the validation and test sets with the minimum and maximum values found on the training set.

To account for sample imbalance, we weigh the error contributions based on the number of samples in each class and average them. Thus, for the test error, we have 50% of the error from each class of Table II.

Over the training set, we use the RMSProp optimization method [26] to minimize the binary cross-entropy loss. We trained for a maximum of 200 epochs with early stopping if there was no reduction in the validation set loss over 10 consecutive epochs. We implemented all the experiments in Keras (version 2.2) using default parameters. All training was performed on an NVIDIA DGX-1 platform with 8 V100 32GB GPUs.

III. DATASET

This retrospective study was approved by the Geisinger Institutional Review Board and performed with a waiver of consent.

TABLE II: Demographics table of 31,278 EHR samples.

	Survival	
	< 1 year	≥ 1 year
Count	4,977	26,301
Male (%)	50	56
Smoker (%)	65	59
Age (years)	73 ± 13	63 ± 16
Heart Rate (bpm)	81 ± 16	73 ± 14
EF (%)	51 ± 14	55 ± 10
LDL (mg/dL)	85 ± 32	93 ± 32
Diastolic Press. (mm[Hg])	66 ± 14	72 ± 13
Systolic Press. (mm[Hg])	124 ± 23	131 ± 21

A. Electronic Health Records

At the time of the study, Geisinger’s echocardiography database contained 594,862 studies from 272,280 unique patients performed over 19 years (February 1998 to September 2018). Each study included patient identifiers, date, and a findings report. Geisinger’s Phenomics Initiative database has modeled these study data into tabular format with 480 human-derived echocardiography measurements.

We retrieved the closest (before or after) fasting LDL, HDL, blood pressure, heart rate, and weight measurements that were not taken at the time of the Echocardiography study within a six-month window. When no measurement was available in that time window, we set the variable as missing. ICD-10 diagnostic codes were formatted as indicator variables that were matched against the date of echocardiography.

All measurements were cleaned from physiologically out of limit values, which may be caused by input errors. In cases where no limits could be defined for a measurement, we removed extreme outliers that met two rules: 1) Value beyond the mean plus or minus three standard deviations and 2) Value below the 25th percentile minus 3 interquartile ranges or above the 75th percentile plus 3 interquartile ranges. The outlier values were set as missing.

To support our models, we also needed to deal with missing values. We filled in the missing data with two steps. First, we conducted a time interpolation to fill in missing measurements using all available studies of an individual patient, i.e., missing values in between echocardiography sessions were linearly interpolated if complete values were found in adjacent echocardiograms acquired before and after the study with a missing value. Then, we kept 115 out of the 480 measurements because they were the most commonly measured with less than 90% missing values. This enabled us to conduct a robust Multiple Imputation by Chained Equations (MICE) [27].

After imputation of the continuous measurements, we imputed the missing diastolic function (which is either normal, abnormal or graded from 1 to 3 in severity) assessment by training a logistic regression classifier (One-vs-All) using 278,160 studies where diastolic function was known. We coded the reported diastolic function in an ordinal fashion with -1 for normal, 0 for dysfunction (but no grade reported), and 1, 2 and 3 for diastolic dysfunction grades I, II, and III, respectively. We calculated the patient’s age and survival time from the date of the echocardiogram. The patient status (dead/alive) was based on the last known living encounter

or confirmed death date, which is regularly checked against national death index databases in our system.

B. Echocardiography videos

An Echocardiography study consists of typically 20–40 ultrasound videos containing multiple views of the heart and vessels with different orientations. We refer to [16] for details in the video extraction and view labeling procedure.

From the echocardiography exams, we kept only the parasternal long axis view since 1) this view is regarded as the most useful view by cardiologists due to being able to capture a large part of the heart’s anatomy in a single view, 2) in our earlier investigations, this view gave the best performance for predicting the risk of one-year mortality [16], and 3) including additional videos remained computationally challenging because of the ratio of available samples vs number of parameters to train.

We linearly interpolated all raw videos to a time resolution of 30 frames per second. We then cropped/padded each video to 60 frames (2 seconds).

C. Clinical and Video Data Merge

We linked the clinical data (CD) and imaging data, and discarded any unlinked data. We gathered 31,278 videos from 26,793 patients. The CD variables were age, smoking status (ever smoked), sex, diastolic pressure, systolic pressure, heart rate, height, weight, low-density lipoprotein (LDL), and high-density lipoprotein (HDL). Finally, we removed studies with less than 1 year of follow-up. Refer to Table II for a summary of the merged dataset.

IV. RESULTS AND DISCUSSION

We begin with a discussion of the most significant features in section IV-A. We then proceed with a discussion of risk models for individual features in section IV-B, and a comparison of the different models in section IV-C.

A. Significant features

We summarize the results for the most significant features for the different models in Table III. As expected for a survival model, age dominates all other features in the basic CD model. Age still dominates even after considering measurements derived from the videos (CD+EDM). Yet, heart rate dominates age in the full model, while it remains the second most important clinical factor in the basic CD and CD+EDM models. Weight, diastolic pressure, and systolic pressure complete the top 5 clinical factors that produced the highest prediction weights. These clinical features are well known and strongly support the interpretability of our results.

Without looking at the video, from the echocardiography measurements (EDM), the Tricuspid Regurgitation Maximum Velocity (TRMV) was the most significant measurement. In fact, the TRMV replaced the systolic pressure from the list of the top 5 clinical features in the combined CD+EDM model. Here, in terms of contributions to the mortality risk, we note that the TRMV measures the maximum velocity of

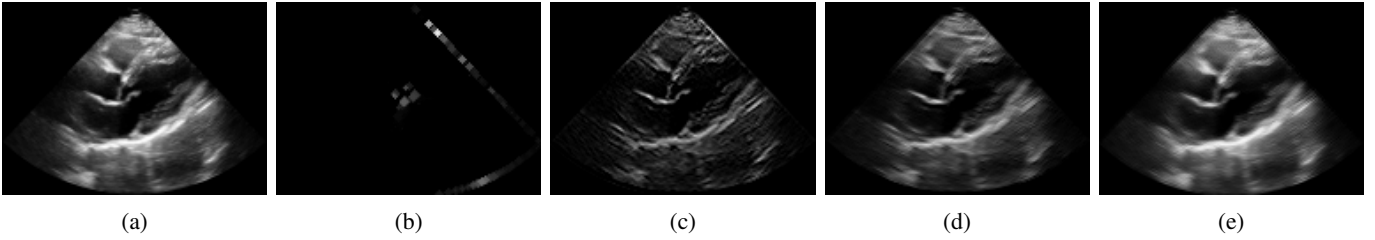


Fig. 3: Example of low-level features extracted from the parasternal long axis view. In this example, we show the outputs from the four feature maps produced by Conv1. The feature maps represent outputs produced using 3x3 kernels and ReLU activation functions. (a) Original image. (b) First feature map, enhanced with a dilation operation for illustration purposes. (c) Second feature map. (d) Third feature map. (e) Fourth feature map.

blood flowing backwards from the right ventricle into the right atrium, which is an indirect measure of pulmonary artery systolic pressure and thus a marker of pulmonary hypertension. Pulmonary hypertension is highly correlated to mortality, as previously discussed in detail in [1], and thus this further supports clinical interpretability of the model.

For the combined model, the video analysis system was the most significant feature. Unfortunately, it is difficult to provide a clinical interpretation of exactly what is being measured by the video analysis system. At the lower layers, we do expect the video analysis system to extract low level features. In our analysis of video outputs from the lower levels, we have found that lower layers do extract cardiac wall features. To show this, we present sample results from the first four features maps generated by Conv1 in 3. The output images from Figs 3(b)-(e) vary significantly. Yet, in Fig. 3(b), we can see the extraction of specific bright points over the aortic valve (center), as well as irrelevant artifacts from the periphery of the scan. We expect that the irrelevant artifacts from the periphery will be rejected by higher layers. In Fig. 3(c), we can see that the cardiac walls are enhanced while the background is suppressed. Cardiac wall enhancement is less pronounced in Fig. 3(d). On the other hand, Fig. 3(e) looks very similar to the input. Hence, it is clear that interesting features from Fig. 3(e) can only be extracted at higher layers.

TABLE III: Feature importance based on the largest weights extracted for the different models. The weights represent averages over 5 runs. LVIDd refers to the left ventricular internal diastolic dimension. AI dec slope refers to the aortic insufficiency deceleration slope.

	CD (no EDM or Video)	EDM	CD+ EDM (no Video)	Video+ CD+ EDM
PL view video	-	-	-	3.86
Heart Rate	2.63	-	1.91	1.72
Age	3.40	-	2.84	1.36
Tricuspid RMV	-	1.80	1.58	1.09
Diastolic Pressure	1.63	-	1.40	0.96
AI dec slope	-	1.20	-	-
Ejection Fraction	-	1.82	-	-
End Systolic Vol	-	1.45	-	-
LVIDd	-	1.43	-	-
Systolic Pressure	1.38	-	-	-
Weight	1.64	-	1.93	-

B. Risk model assessment for individual features

We present risk models for the most relevant clinical features for the full model in Fig. 4. Our risk models include the most significant features discussed in section IV-A as well as some measures that are routinely used in clinical diagnosis and prognosis. Since we are using the full model, it is important to note that our separable interpretations will have to be combined together for the final risk assessment.

We begin with the age factor as a predictor in the CD+EDM model (see Fig. 4(a)). It is clear that mortality increases with age as evidenced by the histogram differences between the two populations (survivors versus non-survivors). In fact, with a weight coefficient of 2.84 (see Table III), we have a 17-fold increase in the odds ratio (probability of dying within a year), when going from an age of 18 to 110. The risk function appears to follow a near linear trend from 40 to 80.

Increased heart rates lead to significant risk increases as shown in Fig. 4(d). Since these measurements are taken from patients at rest, a low resting heart rate may indicate a physically active and therefore generally healthier person, whereas a high rate may be a marker of arrhythmias and/or heart failure.

Extreme low weight gave the highest risk in Fig. 4(e). From low to average weight, we observe that the risk also drops sharply. The risk drops to the lowest value for obese patients. The trend from average to high weight, while appearing to be counter-intuitive, is compatible with the “obesity paradox” noted in multiple prior studies (see [28]). An additional possible explanation is that low weight is a high risk factor

TABLE IV: Multi-modal model performance. For each method and data combination, we present the average AUC and standard deviation based on 5 independent runs. IMNN (Interpretable Multimodal Neural Network) refers to the proposed method. The CD model does not include EDM or Video features. All 3 refers to Video+CD+EDM.

Model Input	IMNN (proposed)	Logistic Regression	Random Forest	XGBoost
CD	0.78 (0.01)	0.79 (0.01)	0.81 (0.00)	0.81 (0.01)
EDM	0.76 (0.01)	0.74 (0.02)	0.77 (0.01)	0.77 (0.01)
Video	0.73 (0.02)	-	-	-
CD+EDM	0.82 (0.01)	0.81 (0.01)	0.81 (0.01)	0.82 (0.01)
All 3	0.82 (0.01)	-	-	-

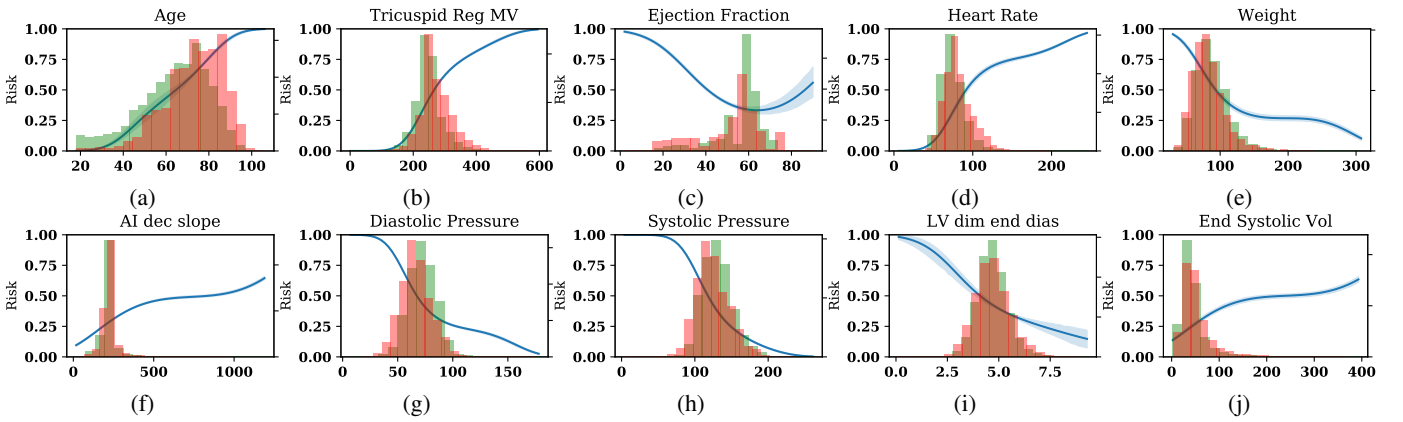


Fig. 4: Full model risk functions (blue) with normalized histograms of survivors (light green) and non-survivors (red orange). When the two histograms overlap, the histograms appear light brown. (a) Age risk plots. (b) Tricuspid regurgitation maximum velocity (TRMV) plots. TRMV is measured in cm/s. (c) physician reported left ventricular ejection fraction in %, (d) heart rate in beats per minute, (e) weight in kilograms, (f) aortic insufficiency deceleration slope (AI dec slope) in cm/s^2 , (g) diastolic and (h) systolic blood pressure in mm Hg, (i) left ventricular internal dimension at end-diastole in cm, and (j) left ventricular end systolic volume in ml. The uncertainty in the risk functions are derived from the 5 results across the 5 runs.

for short term (<1 year) mortality and high weight may have a higher association with longer term mortality.

We have decreasing risk trends for larger values of systolic and diastolic pressure (see Figs. 4(g)-(h)). Though lower blood pressure being associated with higher risk is counterintuitive, two explanations are plausible. First, a high blood pressure does not lead to 1-year mortality but rather leads to longterm cumulative effects such as renal and heart failure that result in longer-term increased mortality. Second, low blood pressure may be a marker of cardiac decompensation. Full understanding of this trend will require further study and also accounting for many medications known to affect blood pressure.

We have a strong, increasing trend for increases in the tricuspid regurgitation maximum velocity (TRMV, see Fig. 4(b)). Based on our prior discussion on the TRMV, this trend is clearly to be expected and compatible with pulmonary hypertension being strongly linked to mortality.

From Fig. 4(f), we can see that higher values of the aortic insufficiency deceleration slope demonstrate the relationship between severity of aortic valve regurgitation/insufficiency and mortality [29]. On the other hand, from Fig. 4(i), we see a counter-intuitive trend for the left ventricular internal dimension that suggests a lower value is associated with a higher risk of death, which is opposite of what is expected [30]. However, the histograms in Fig. 4(i) show little difference between the surviving and non-surviving populations. Hence, it is not a surprise that this feature was not found to be significant and the trend likely is spurious. From Fig. 4(j), we observe that the left ventricular end systolic volume, which is a better marker of ventricular size than the LV internal dimension described above, follows the expected trend of worsening mortality for higher values.

A mixed trend is observed for the left ventricular ejection fraction (EF) in Fig. 4(c). Here, we note that the EF is the percentage of blood that leaves the heart chambers during contraction. From a minimum risk at 65%, the odds ratio

indicates a two-fold increase in risk at an EF of 10% or lower, and a 56% risk increase for an EF of 85% or higher. For low risk cases, the EF risk function agrees with standard clinical interpretation and the current American Heart Association guidelines (reviewed as of May 31, 2017) for a normal EF, which is between 50% and 70%. Increased risk with high EF may be a marker of a hyperdynamic heart failure with preserved ejection fraction or additional pathologic factors known to elevate EF such as mitral regurgitation or concentric hypertrophic remodeling (either genetic or acquired secondary to hypertension).

C. Model results

Our model results are summarized in Table IV. First, we note that the performance of the CD+EDM with Random Forest model does not match the performance reported in [1] (0.81 vs 0.84 AUC). We determined that the source of this difference relates to the specific subset of patients included in this analysis (selected based on the availability of the raw echocardiography videos). While the exact cause of the bias is unknown, we do note that our current population, compared to that of [1], did exhibit several demonstrable differences in features, such as 1) increased prevalence of dead patients within a year (16% vs 12%); 2) larger proportion of patients with mild Tricuspid (33% vs 26%) and Mitral (33% vs 25%) Regurgitation; and 3) larger percentages of patients with diagnoses of chronic kidney disease (19% vs 13%), hypertension (54% vs 47%) and heart failure (16% vs 13%).

Even with our limited statistics from 5 independent runs, we conducted 5 paired t-tests with $\alpha = 0.01/5$ to test for AUC average differences among modalities (CD vs EDM, CD vs Video) and the use of additional modalities (CD vs CD+EDM, CD+EDM vs CD+EDM+Video (“All”). We found no significant differences among the different single modalities. Yet, we found a significant increase in the AUC

when multiple modalities were utilized. In particular, we found a significant increase from CD (AUC average = 0.78) to CD+EDM (AUC average = 0.82). On the other hand, we did not find significant differences between the CD+EDM model and the CD+EDM+Video model. Future work can likely improve upon this by adding more computational complexity with the addition of many more echocardiographic views to the models, which will likely result in improved accuracy with appropriate increases in sample size to balance additional parameters that need to be trained. In addition, we acknowledge that the interaction between variables is not addressed by the proposed model and that the separable approach assumes independent features. However, this work can be extended to cover conditional transformations (e.g., see [31]) or include the multiplication of factors as in traditional general linear models analysis to account for interactions in future work.

Overall, the full multi-modal model performed as well as any other model. For CD+EDM, most models performed as well as the full model. However, it is important to note that the complex non-linear relationships of Fig. 4 are only possible through using our interpretable model. Logistic regression only allows linear models, which are clearly inadequate for many clinical features (see Fig. 4). On the other hand, while we can also assess feature importance with Random Forest and XGBoost, there is no clear understanding of what any single feature contributes to the risk as has been demonstrated with the newly proposed interpretable model.

V. CONCLUSION

This paper introduces interpretable models for risk assessment in clinical scenarios that demand multi-modal data inputs. Through the use of separable, non-linear models, we are able to quantify the contributions of individual clinical factors to the overall risk, assuming the remaining factors remain constant. The approach allows us to visualize complex non-linear relationships between changes in each factor and other non-linear models. Overall, the proposed interpretable models matched the performance of more complex non-linear methods and thus demonstrate significant potential for expanding the use of neural networks in medicine.

VI. ACKNOWLEDGEMENT

This project was also funded, in part, under a grant with the Pennsylvania Department of Health (#SAP 4100070267).

REFERENCES

- [1] M. D. Samad, A. Ulloa, G. J. Wehner, L. Jing, D. Hartzel, C. W. Good, B. A. Williams, C. M. Haggerty, and B. K. Fornwalt, "Predicting survival from large echocardiography and electronic health record datasets: Optimization with machine learning," *JACC: Cardiovascular Imaging*, 2018.
- [2] R. W. Foley, R. M. Maweni, L. Gorman, K. Murphy, D. J. Lundon, G. Durkan, R. Power, F. O'Brien, K. J. O'Malley, D. J. Galvin *et al.*, "European randomised study of screening for prostate cancer (erspc) risk calculators significantly outperform the prostate cancer prevention trial (pcpt) 2.0 in the prediction of prostate cancer: a multi-institutional study," *BJU international*, vol. 118, no. 5, pp. 706–713, 2016.
- [3] L. A. Allen, D. D. Matlock, S. M. Shetterly, S. Xu, W. C. Levy, L. B. Portalupi, C. K. McIlvennan, J. H. Gurwitz, E. S. Johnson, D. H. Smith *et al.*, "Use of risk models to predict death in the next year among individual ambulatory patients with heart failure," *JAMA cardiology*, vol. 2, no. 4, pp. 435–441, 2017.
- [4] A. S. Panayides, M. S. Pattichis, S. Leandrou, C. Pitrís, A. Constantinidou, and C. Pattichis, "Radiogenomics for precision medicine with a big data analytics perspective," *IEEE journal of biomedical and health informatics*, vol. early access, 2018. [Online]. Available: <https://ieeexplore.ieee.org/document/8588324>
- [5] C. Bonner, M. A. Fajardo, S. Hui, R. Stubbs, and L. Trevena, "Clinical validity, understandability, and actionability of online cardiovascular disease risk calculators: Systematic review," *Journal of medical Internet research*, vol. 20, no. 2, 2018.
- [6] M. W. Kattan, K. R. Hess, M. B. Amin, Y. Lu, K. G. Moons, J. E. Gershenwald, P. A. Gimotty, J. H. Guinney, S. Halabi, A. J. Lazar *et al.*, "American joint committee on cancer acceptance criteria for inclusion of risk models for individualized prognosis in the practice of precision medicine," *CA: a cancer journal for clinicians*, vol. 66, no. 5, pp. 370–374, 2016.
- [7] D. Bertsimas and J. Dunn, "Optimal classification trees," *Machine Learning*, vol. 106, no. 7, pp. 1039–1082, 2017.
- [8] Z. Cui, W. Chen, Y. He, and Y. Chen, "Optimal action extraction for random forests and boosted trees," in *Proceedings of the 21th ACM SIGKDD International Conference on Knowledge Discovery and Data Mining*. ACM, 2015, pp. 179–188.
- [9] G. Tolomei, F. Silvestri, A. Haines, and M. Lalmas, "Interpretable predictions of tree-based ensembles via actionable feature tweaking," in *Proceedings of the 23rd ACM SIGKDD International Conference on Knowledge Discovery and Data Mining*. ACM, 2017, pp. 465–474.
- [10] G. Litjens, T. Kooi, B. E. Bejnordi, A. A. A. Setio, F. Ciompi, M. Ghahfarooian, J. A. Van Der Laak, B. Van Ginneken, and C. I. Sánchez, "A survey on deep learning in medical image analysis," *Medical image analysis*, vol. 42, pp. 60–88, 2017.
- [11] B. Shickel, P. J. Tighe, A. Bihorac, and P. Rashidi, "Deep ehr: a survey of recent advances in deep learning techniques for electronic health record (ehr) analysis," *IEEE journal of biomedical and health informatics*, vol. 22, no. 5, pp. 1589–1604, 2018.
- [12] L. Yu, Y. Guo, Y. Wang, J. Yu, and P. Chen, "Segmentation of fetal left ventricle in echocardiographic sequences based on dynamic convolutional neural networks," *IEEE Transactions on Biomedical Engineering*, vol. 64, no. 8, pp. 1886–1895, 2017.
- [13] J. Zhang, S. Gajjala, P. Agrawal, G. H. Tison, L. A. Hallock, L. Beussink-Nelson, M. H. Lassen, E. Fan, M. A. Aras, C. Jordan *et al.*, "Fully automated echocardiogram interpretation in clinical practice: feasibility and diagnostic accuracy," *Circulation*, vol. 138, no. 16, pp. 1623–1635, 2018.
- [14] H. Chen, Q. Dou, D. Ni, J.-Z. Cheng, J. Qin, S. Li, and P.-A. Heng, "Automatic fetal ultrasound standard plane detection using knowledge transferred recurrent neural networks," in *International Conference on Medical Image Computing and Computer-Assisted Intervention*. Springer, 2015, pp. 507–514.
- [15] H. Chen, L. Wu, Q. Dou, J. Qin, S. Li, J.-Z. Cheng, D. Ni, and P.-A. Heng, "Ultrasound standard plane detection using a composite neural network framework," *IEEE transactions on cybernetics*, vol. 47, no. 6, pp. 1576–1586, 2017.
- [16] A. Ulloa, L. Jing, C. W. Good, D. P. vanMaanen, S. Raghunath, J. D. Suever, C. D. Nevius, G. J. Wehner, D. Hartzel, J. B. Leader *et al.*, "A deep neural network predicts survival after heart imaging better than cardiologists," *arXiv preprint arXiv:1811.10553*, 2018.
- [17] J. Long, E. Shelhamer, and T. Darrell, "Fully convolutional networks for semantic segmentation," in *Proceedings of the IEEE conference on computer vision and pattern recognition*, 2015, pp. 3431–3440.
- [18] V. Badrinarayanan, A. Kendall, and R. Cipolla, "Segnet: A deep convolutional encoder-decoder architecture for image segmentation," *arXiv preprint arXiv:1511.00561*, 2015.
- [19] O. Ronneberger, P. Fischer, and T. Brox, "U-net: Convolutional networks for biomedical image segmentation," in *International Conference on Medical image computing and computer-assisted intervention*. Springer, 2015, pp. 234–241.
- [20] M. Gevrey, I. Dimopoulos, and S. Lek, "Review and comparison of methods to study the contribution of variables in artificial neural network models," *Ecological modelling*, vol. 160, no. 3, pp. 249–264, 2003.
- [21] M. T. Ribeiro, S. Singh, and C. Guestrin, "Why should i trust you?: Explaining the predictions of any classifier," in *Proceedings of the 22nd ACM SIGKDD international conference on knowledge discovery and data mining*. ACM, 2016, pp. 1135–1144.
- [22] S. Ioffe and C. Szegedy, "Batch normalization: Accelerating deep network training by reducing internal covariate shift," *arXiv preprint arXiv:1502.03167*, 2015.

- [23] J. Friedman, T. Hastie, and R. Tibshirani, *The elements of statistical learning: Data Mining, Inference, and Prediction*, 2nd ed. New York: Springer series in statistics New York, 2009.
- [24] L. Breiman, "Random forests," *Machine learning*, vol. 45, no. 1, pp. 5–32, 2001.
- [25] T. Chen and C. Guestrin, "Xgboost: A scalable tree boosting system," in *Proceedings of the 22nd acm sigkdd international conference on knowledge discovery and data mining*. ACM, 2016, pp. 785–794.
- [26] Y. Dauphin, H. de Vries, and Y. Bengio, "Equilibrated adaptive learning rates for non-convex optimization," in *Advances in neural information processing systems*, 2015, pp. 1504–1512.
- [27] S. v. Buuren and K. Groothuis-Oudshoorn, "mice: Multivariate imputation by chained equations in r," *Journal of statistical software*, pp. 1–68, 2010.
- [28] C. J. Lavie, A. De Schutter, P. Parto, E. Jahangir, P. Kokkinos, F. B. Ortega, R. Arena, and R. V. Milani, "Obesity and prevalence of cardiovascular diseases and prognosis: the obesity paradox updated," *Progress in cardiovascular diseases*, vol. 58, no. 5, pp. 537–547, 2016.
- [29] W. A. Zoghbi, M. Enriquez-Sarano, E. Foster, P. A. Grayburn, C. D. Kraft, R. A. Levine, P. Nihoyannopoulos, C. M. Otto, M. A. Quinones, H. Rakowski *et al.*, "Recommendations for evaluation of the severity of native valvular regurgitation with two-dimensional and doppler echocardiography," *Journal of the American Society of Echocardiography*, vol. 16, no. 7, pp. 777–802, 2003.
- [30] R. M. Lang, M. Bierig, R. B. Devereux, F. A. Flachskampf, E. Foster, P. A. Pellikka, M. H. Picard, M. J. Roman, J. Seward, J. Shanewise *et al.*, "Recommendations for chamber quantification," *European journal of echocardiography*, vol. 7, no. 2, pp. 79–108, 2006.
- [31] T. Hothorn, T. Kneib, and P. Bühlmann, "Conditional transformation models," *Journal of the Royal Statistical Society: Series B (Statistical Methodology)*, vol. 76, no. 1, pp. 3–27, 2014.